Experimental Observation and Computational Study of the Spin-gap Excitation in $Ba_3BiRu_2O_9$

C. D. Ling*, Z. Huang, B. J. Kennedy
School of Chemistry, The University of Sydney, Sydney 2006, Australia

S. Rols, M. R. Johnson, M. Zbiri
Institut Laue Langevin, 71 avenue des Martyrs, Grenoble 38042, France

S. A. J. Kimber, J. Hudspeth
European Synchrotron Radiation Facility, 71 avenue des Martyrs, Grenoble 38042, France

D. T. Adroja
ISIS Facility, Science and Technology Facilities Council, Rutherford Appleton Laboratory, Didcot OX11 0QX, United Kingdom and Highly Correlated Matter Research Group, Physics Department, University of Johannesburg, P.O. Box 524, Auckland Park 2006, South Africa

K. C. Rule, M. Avdeev
The Bragg Institute, ANSTO, PMB 1, Menai 2234, Australia

P. E. R. Blanchard
Canadian Light Source, 44 Innovation Boulevard, Saskatoon, SK S7N 2V3, Canada

(Dated: October 11, 2016)

$Ba_3BiRu_2O_9$ is a 6H-type perovskite compound containing face-sharing octahedral M_2O_9 (M = Ir, Ru) dimers, which are magnetically frustrated at low temperatures. On cooling through $T^* = 176$ K, it undergoes a pronounced magnetostructural transition which is not accompanied by any change in space group symmetry, long-range magnetic ordering, or charge ordering. Here, we report the first direct evidence from inelastic neutron scattering that this transition is due to an opening of a gap in the excitation spectrum of dimers of low-spin Ru^{4+} ($S = 1$) ions. X-ray absorption spectroscopy reveals a change in Ru-Ru orbital overlap at T^*, linking the emergence of this spin-gap excitation to the magnetostructural transition. *Ab initio* calculations point to a geometrically frustrated magnetic ground state due to antiferromagnetic inter-dimer exchange on a triangular Ru_2O_9 dimer lattice. X-ray total-scattering data rule out long-range magnetic ordering at low temperatures, consistent with this geometrically frustrated model.

I. INTRODUCTION

Systems exhibiting quantum cooperative phenomena, due to strong coupling between magnetic, electronic and cell parameter degrees of freedom, have been intensively studied over recent years. An important subclass of these is the low dimension quantum magnets, which generally contain structural motifs such as chains, dimers, and geometrically frustrated configurations. Spin-lattice coupling in these compounds result in pronounced magnetoelastic effects such as the spin-Peierls transition in an $S = 1/2$ Ising-chain antiferromagnet [1]. Compounds based on $S = 1/2$ 3d transition-metal cations such as Cu^{2+}, V^{4+}, and Ti^{3+} have been studied most thoroughly, while $S = 1$ systems remain relatively neglected. However, compounds based on $S = 1$ low-spin Ru^{4+} have been reported to show some remarkable properties such as superconductivity in Sr_2RuO_4 [2], non-Fermi-liquid behavior in $La_4Ru_6O_{19}$ [3], and spin-gap (Haldane gap) opening in $Tl_2Ru_2O_7$ [4].

$Ba_3BiIr_2O_9$ [5, 6] and $Ba_3BiRu_2O_9$ [7, 8] are recent examples of low dimension quantum magnetic materials based on low-spin $S = 1/2$ Ir^{4+} and $S = 1$ Ru^{4+} respectively. These isostructural compounds are 6H-type perovskites in the hexagonal space group $P6_3/mmc$ at high temperature, relaxing slightly to the monoclinic $C2/c$ space group below $\sim$ 750 K. They contain face-sharing octahedral M_2O_9 (M = Ir, Ru) dimers which are magnetically frustrated at low temperatures due to the hexagonal arrangement of M_2O_9 dimers within layers and their triangular arrangement from one layer to the next (Fig. 1).

On cooling through $T^* = 74$ K, $Ba_3BiIr_2O_9$ displays the largest magnetoelastic effect known among 5d compounds, with an anisotropic 1.0% negative thermal volume expansion accompanied by a sharp drop in magnetic susceptibility indicative of an antiferromagnetic (AFM) ordering transition and the opening of a spin-gap [6]. The ruthenium analogue displays a similar transition at $T^* = 176$ K, with a smaller (0.1%) volume expansion [8]. Despite these large volume changes, for both compounds there is no deviation from $C2/c$ space group symmetry at T^*, nor is there any evidence for long-range magnetic or charge ordering.

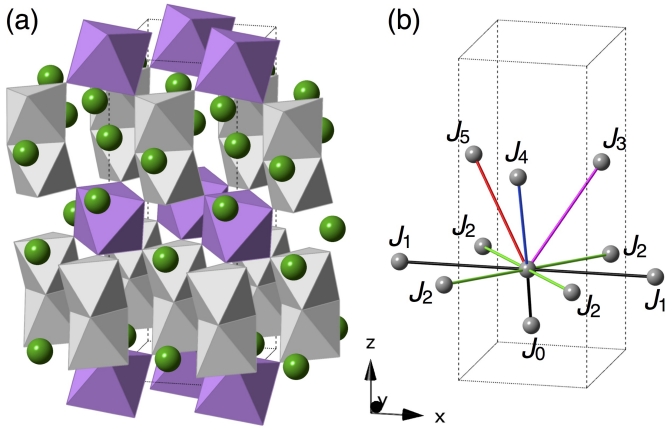

FIG. 1. (a) Structure of $Ba_3BiRu_2O_9$ showing face-sharing Ru_2O_9 octahedral dimers (grey), BiO_6 octahedra (purple), and barium atoms (green). (b) Modelled Ru-Ru magnetic exchange interactions in $Ba_3BiRu_2O_9$ (see Section III.D for details).

The nature of the change in the electronic state at T^* remains elusive. It clearly involves the emergence of local pairwise AFM interactions among Ir/Ru ions, but without long-range order. A cursory examination of the crystal structure immediately suggests that the AFM interactions appear in the face-sharing octahedral M_2O_9 ($M = Ir^{4+}$, Ru^{4+}) dimers, due to direct $M-M$ exchange and/or 90° $M-O-M$ superexchange, and that the absence of long-range order is due to the weakness of the interactions between dimers. However, because the $M-M$ distance of ~ 2.6 Å is extremely short (shorter than found in pure metals), such interactions would normally be expected to appear in a continuous second-order transition well above T^*, and therefore do not appear to be consistent with the observed first-order transitions. This raises the possibility that the pairwise AFM interactions are occurring between, rather than within (or a combination of both), the M_2O_9 dimers. Such inter-dimer interactions would be geometrically frustrated, potentially explaining the first-order nature of the transition and the lack of any experimental evidence for long-range spin ordering.

Inter-dimer interactions would be mediated by bridging BiO_6 octahedra. In this context it is important to note that a magnetoelastic transition is not observed in analogous 6H-type perovskites in which Bi is replaced by other 4+ valent cations ($Ba_3CeIr_2O_9$, $Ba_3PrIr_2O_9$, $Ba_3TbIr_2O_9$ [9]; $Ba_3CeRu_2O_9$, $Ba_3PrRu_2O_9$, $Ba_3TbRu_2O_9$ [10], $Ba_3ZrRu_2O_9$ [11]). This may be related to the fact that the apparent "4+" oxidation state of bismuth is highly unusual: Bi^{4+} usually disproportionates locally into Bi^{3+} and Bi^{5+} due to its energetically unfavourable configuration $4f^{14}5d^{10}6s^1$, as in, *e.g.*, $BaBiO_3$ [12–17]. The disproportionation/charge ordering in this case appears to be inhibited by geometric frustration; we see no evidence for it in structural data, despite the expected strong geometrical/steric effect of the stereochemically active $6s^2$ electron lone pair on Bi^{3+} and its absence on Bi^{5+}. The inherent instability of the electronic state of Bi may thus be another factor in the transitions at T^*.

In this work we report the experimental observation of a spin-gap opening in $Ba_3BiRu_2O_9$ by inelastic neutron scattering. We have used this accurate experimental value for the energy of the excitation to benchmark a series of high-level *ab initio* calculations aimed at determining the electronic nature of the transition at T^* in $Ba_3BiRu_2O_9$, and by analogy the corresponding transition in $Ba_3BiIr_2O_9$.

II. EXPERIMENTAL METHODS

Inelastic neutron scattering (INS) measurements were carried out on the direct-geometry, thermal-neutron time-of-flight spectrometer IN4C at the Institut Laue Langevin (Grenoble, France). An incident wavelength $\lambda_i = 1.11$ Å (E_i=66.4 meV) was selected using a pyrolitic graphite monochromator. 20 g of polycrystalline $Ba_3BiRu_2O_9$ was sealed into a thin aluminium foil that was fixed to the cold tip of the sample stick of a standard orange cryostat. Measurements were performed at 100 K and 200 K, below and above $T^* = 176$ K respectively. The scattering function $S(Q,E)$ was measured in the neutron energy loss mode, in which the setting used in the down-scattering regime leads to a momentum transfer (Q) and energy transfer (E) extending up to 10 $Å^{-1}$ and 60 meV, respectively. Standard corrections including detector efficiency calibration and background subtraction were performed. The data analysis was done using ILL software tools.

Further INS data for $Ba_3BiRu_2O_9$ were subsequently taken on the time-of-flight instrument Merlin at ISIS, in an attempt to access lower-Q regions of the $S(Q,\omega)$ map. Merlin has larger detector coverage in both the horizontal ($\sim 180°$) and vertical ($\pm 30°$) scattering planes. A 20 g powder sample was placed in an envelope of thin aluminium foil (40 mm height and 140 mm length) which was rolled into cylindrical form and inserted inside a thin aluminium cylindrical can (diameter of 40 mm with wall thickness of 0.1 mm). The sample was cooled to the lowest temperature of 5 K using a closed-cycle refrigerator under He-exchange gas to thermalize the sample temperature. Data were collected at various temperatures between 5 and 300 K. The incident neutron energy of 80 meV was selected using a Fermi chopper.

Data were also collected on the thermal triple-axis spectrometer Taipan operated by the Australian Nuclear Science and Technology Organisation (ANSTO). The instrument was aligned with open collimation and a double-focusing monochromator and analyser to ensure high neutron flux at the sample position. The instrument was aligned in the W-configuration with a fixed final energy of $E_f = 14.87$ meV which afforded an energy resolution of ~ 1 meV at the elastic line. The polycrystalline sample was mounted in an annular Al can to ensure $\sim 10\%$ scat-

tering from the sample.Measurements were taken with a closed-cycle cryofurnace over a temperature range of 3-200 K.

Density functional theory (DFT) calculations were performed in the generalised gradient approximation using the Perdew-Burke-Ernzerhof (PBE) exchange-correlation functional in the Vienna *ab initio* simulations package (VASP) version 5.2 [18]. Projector augmented wave (PAW) pseudopotentials [19] were used. The plane wave energy cut-off was 400 eV. Spin-orbit coupling was included in the calculations. All results were converged with respect to this energy cut-off and k-point sampling. Most calculations were performed on a $2 \times 1 \times 1$ supercell ($\sim 12 \times 10 \times 15$ Å) containing 60 atoms for which the k-point grid was $2 \times 2 \times 2$.

Ru L_3-edge x-ray absorption near-edge structure (XANES) spectra for $Ba_3BiRu_2O_9$ were collected on beamline 16A1 at the National Synchrotron Radiation Research Center (NSRRC), Taiwan. [20] Finely ground samples were pressed into pellets and positioned in front of the X-ray beam at a 45° angle in a He-cooled closed-cycle cryostat. Spectra were collected at 298, 200, 176, 169 and 10.5 K in total fluorescence yield (TFY) mode using a Lytle detector. Spectra were collected from -50 eV to + 200 eV relative to the Ru L_3 absorption edge with an energy step-size of 0.2 eV near the absorption edge. The Ru L_3-edge spectra were calibrated against elemental Mo with the maximum in the first derivative of the L_2-edge set to 2625 eV. All XANES spectra were analyzed using the Athena software package. [21] The peak widths were obtained by fitting to a pseudo-Voigt lineshape with an arctan background to fit the edge jump, while intensities were obtained by fitting the spectra to component peaks corresponding to the t_{2g} and e_g states.

X-ray total scattering data were collected on beam line ID15B of the European Synchrotron Radiation Facility (ESRF), Grenoble France. An incident energy of 87 keV was used, and the scattered x-rays were detected using a Mar345 image plate. Temperature control was provided with an Oxford Cryostream, and the sample was placed in a glass capillary, which was rotated rapidly during data collection. An empty capillary was measured to estimate the experimental background. This scattering was scaled to the incident beam intensity and subtracted. Azimuthal integration of the 2D detector images was performed using Fit2D, [22] and data were transformed to real space using PDFGetx3. [23] Modelling was performed in real space using PDFGui. [24]

III. RESULTS

A. Inelastic Neutron Scattering

The primary goal of the inelastic neutron scattering (INS) experiments was to directly measure the energy of the spin-gap excitation in $Ba_3BiRu_2O_9$, previously estimated from physical property measurements. Fig. 2 shows the color-coded Bose-factor corrected $S(Q, E)$ maps of the INS intensity obtained on Merlin for $Ba_3BiRu_2O_9$ above, and at three temperatures below, $T^* = 176$ K. A spin-gap excitation peak is clearly seen to emerge at low Q below T^*. The same peak was seen in data collected on IN4 (not shown). Fig. 3 shows scans taken through the peak at $E_f = 14.87$ meV and $S_2 = 15.5\ °2\theta$ ($|\ Q\ | = 2.06$ Å^{-1} at $E = 36$ meV) on Taipan at 3 and 200 K. The peak was fitted to a Gaussian with respect to energy transfer to yield a spin-gap value $E_{exp} = 36.03 \pm 0.14$ meV. This compares favourably to previous estimates based on analysis of heat capacity (16.6 ± 0.5) and magnetic susceptibility (21.3 ± 0.2) data[8].

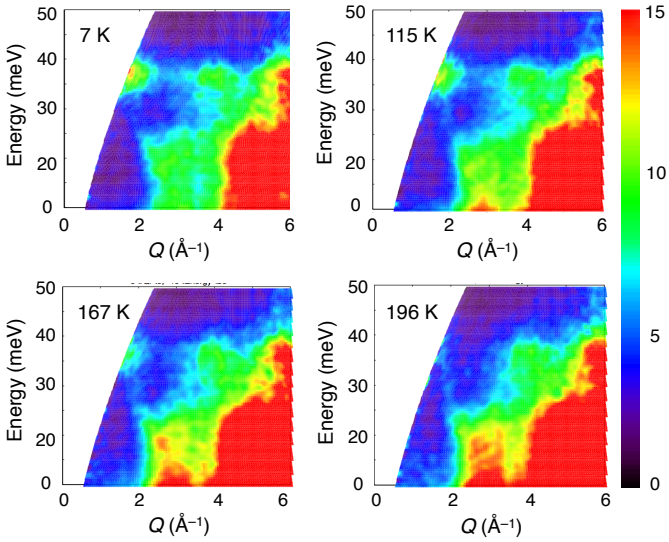

FIG. 2. Color-coded Bose-factor corrected S(Q, E) maps of the inelastic neutron scattering of $Ba_3BiRu_2O_9$ taken on Merlin at ISIS above, and at three temperatures below, $T^* = 176$ K. A magnetic excitation emerges below T^* at low-Q and an energy transfer of 36 meV. The color scale at right shows intensity (arbitrary units).

Fig. 3(b) shows the temperature dependence of this peak intensity, fit to an order parameter $((T_c - T)/T_c)^{2\beta}$, yielding $T_c = 175$ K and $\beta = 0.204$, perfectly consistent with $T^* = 176$ K. Neither the energy nor the linewidth of the excitation peak change as a function of temperature, within the resolution of our measurements. We note that while the magnetostructural transition takes place over a very narrow temperature range and is definitively first-order[8], the excitation observed by INS is not; this is consistent because it is only after ordering magnetically (which happens quickly) that the singlet-triplet gap can begin to open.

An analogous spin-gap excitation was not observed for $Ba_3BiIr_2O_9$; however, this is unsurprising given the very high neutron absorption cross-section of Ir and the extremely rapid fall-off of the Ir^{4+} magnetic form-factor, both of which obscure magnetic scattering intensity.

An isolated antiferromagnetic (AFM) dimer of $S = 1$

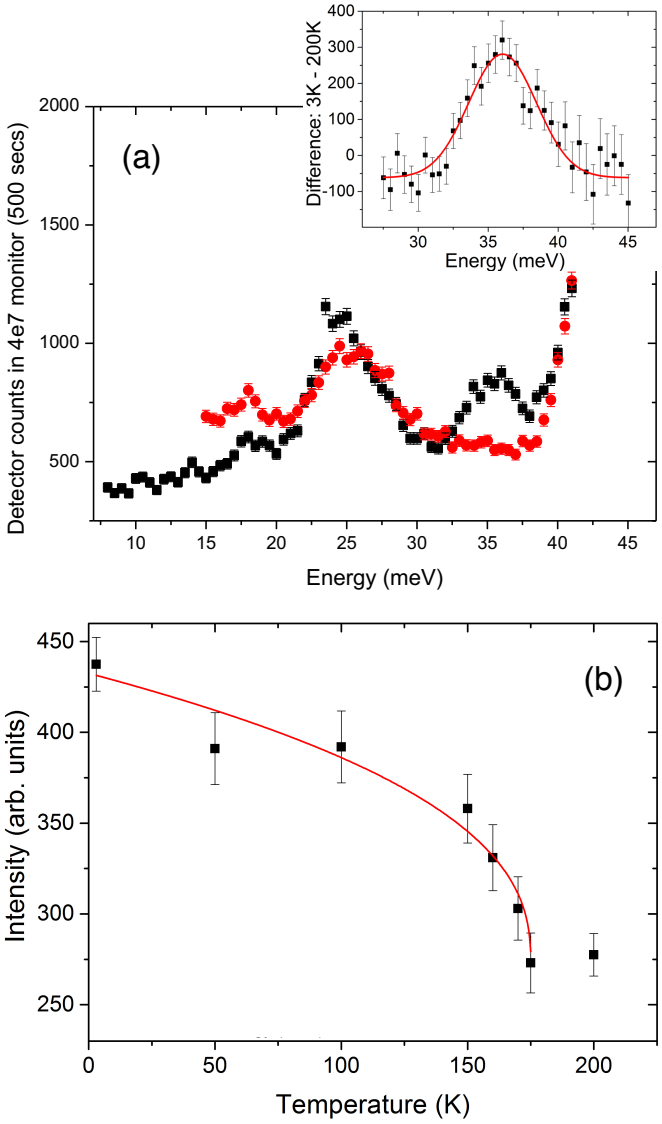

FIG. 3. Inelastic neutron scattering from $Ba_3BiRu_2O_9$, measured on Taipan at ANSTO. (a) Shows low-Q scans above (200 K, red) and below (3 K, black) $T^* = 176$ K. The inset shows the difference (3 K - 200 K) fit to a Gaussian centred at $E_{exp} = 36.03 \pm 0.14$ meV. (b) The intensity of this peak as a function of temperature, fit to an order parameter (see text for details).

Ru^{4+} ions with intradimer exchange J_0 will have a non-magnetic $S_{dimer} = 0$ singlet ground state at an energy of $E = -2J_0$, and magnetic $S_{dimer} = 1$ triplet and $S_{dimer} = 2$ quintet excited states at energies $E = -J_0$ and $E = J_0$ respectively. Since INS can only probe gaps with $\Delta S_{dimer} = 1$, our experimental observation must be either the singlet-triplet ($\Delta E = J_0$) or triplet-quintet ($\Delta E = 2J_0$) excitations. Given that we only observe one energy excitation within the energy window of our experiments, this is presumably the lower energy singlet-triplet case.

From previous experiments, no magnetic Bragg peaks were observed in neutron powder diffraction data for $Ba_3BiRu_2O_9$ [8] below T^*, indicating a lack of (observable) long range magnetic ordering. A model for diffuse scattering for liquids/gases etc., which is generally used for dimer systems, was therefore used to fit the INS data. Assuming the dimer state can be described by the wavefunctions $|s_1, s_2, M\rangle$ at the energy transfer corresponding to the spin gap, the intensity of scattered neutrons is given by [25]:

$$I \propto \exp(-\frac{\Delta_0}{k_B T}) \exp(-2W) f^2(Q) \mathbf{M} (1 - \frac{\sin(QR)}{QR}) \quad (1)$$

where Δ_0 is the spin gap, $\exp(-2W)$ is the Debye-Waller factor, $f(Q)$ the magnetic form factor and $\mathbf{M}$ is the matrix element describing the transition, and R is the metal-metal distance. In this case, we wish to study whether the effect is due to intra-dimer of inter-dimer alignment. The last term describes interference effect as a result of the metal-metal distance in the dimer.

An integrated intensity slice was taken over the energy transfer range 32-42 meV of the Merlin data at 7 K and fitted to Equation (1) from $Q = 1.6$ Å^{-1} to $Q = 2.4$ Å^{-1}. Larger Q values were excluded because the phonon background became significant. The form factor for Ru^{5+} [26] was used to perform the analysis, as there is no available experimental form factor for Ru^{4+}, and a phonon background was modeled of the form $xQ^2 + y$. Two alternative fits to determine the Ru-Ru distance were performed: one starting from the experimental intra-dimer Ru-Ru distance of 2.6 Å; and another starting from the (average) experimental inter-dimer distance of 5.9 Å[8]. The former converged to an intra-dimer distance of R = 2.61±0.01 Å, and the latter to R = 5.5±0.2 Å. Note that the second discrete peak near $Q = 4$ Å^{-1} is a phonon peak due to the aluminum sample holder. The intra-dimer model, shown in Fig. 4, produced the better fit to the low Q intensity. However, it should be acknowledged that without very low Q data, the inter-dimer model cannot be conclusively ruled out.

Our INS data thus quantify the energy of the spin-gap excitation as $E_{exp} = 36.03 \pm 0.14$ meV, and associate it with a change in the electronic state of Ru^{4+} dimers in face-sharing Ru_2O_9 bi-octahedra.

B. X-ray Absorption Spectroscopy

Assigning the spin-gap in $Ba_3BiRu_2O_9$ to a singlet-triplet excitation within Ru^{4+} dimers means that its appearance below T^* should be reflected in a change to the electronic structure of those dimers. Given that there is also a structural change below T^* that expands the crystallographic c axis along which Ru-Ru dimers are aligned, the most obvious change should be to the direct interaction between t_{2g} orbitals of neighboring Ru^{4+}. In order to test this, we collected x-ray absorption spectra at the Ru L_3-edge, and analyzed the x-ray absorption

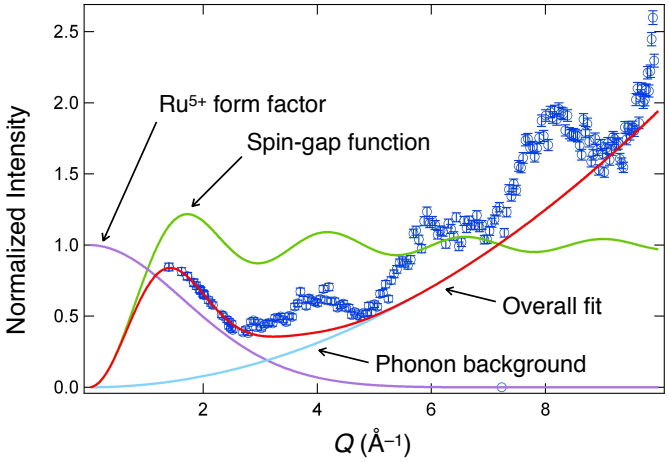

FIG. 4. Integrated intensity over the energy transfer range 32-42 meV of the Merlin data at 7 K, fit to equation (1). Components of the fit are labelled (see text for details). The oscillations at higher Q in the experimental data (blue circles) are non-magnetic (phonon) peaks due partly to the aluminum sample holder.

.

near-edge structure (XANES). This edge corresponds to a dipole-allowed transition of a $2p_{3/2}$ electron into unoccupied 4d states. Information on the oxidation state and local chemical environment of Ru can be inferred as the Ru L_3-edge directly probes the Ru 4d bonding states.

Spectra collected at various temperatures are shown in Figure 5(a). The lineshape and absorption energy of the Ru L_3-edge of is characteristic of 6-coordinate Ru^{4+}. [27, 28] There are two features, corresponding to the t_{2g} (low energy peak) and e_g (high energy peak) orbitals. The intensity of the t_{2g} peak is less than that of the e_g peak due to the Ru t_{2g} states being partially occupied in low-spin Ru^{4+}. Upon cooling $Ba_3BiRu_2O_9$ to 10 K, the relative intensity of the t_{2g} peak increases, as shown in Figure 5(b). The intensity of the Ru L_3-edge is directly proportional to the number of unoccupied 4d states. The Ru L_3-edge results suggest that the number of unoccupied Ru t_{2g} states increases rapidly upon cooling through $T^* = 176$ K. As there is no increase in the Ru L_3-edge absorption energy, any increase in the oxidation state of Ru would have to be very small. [29] The greater number of unoccupied t_{2g} states at low temperature therefore suggests that they are becoming more localized; *i.e.*, there is less direct overlap between t_{2g} states of neighboring Ru^{4+} sites within dimers in the gapped state below T^*. This is consistent with a reinforcement of intra-dimer magnetic exchange below T^*, and therefore with the INS results.

C. *Ab initio* Calculations

Our unambiguous and precise measurement of the spin-gap energy provides an experimental reference point for *ab initio* calculations of the magnetic exchange in-

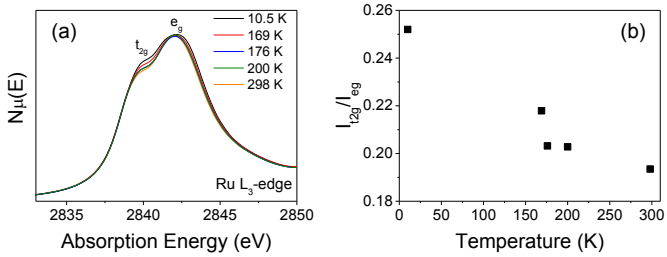

FIG. 5. (a) XANES data taken at the Ru L_3-edge for $Ba_3BiRu_2O_9$ at different temperatures. (b) Integrated t_{2g}/e_g intensity ratio as a function of temperature.

teractions in $Ba_3BiRu_2O_9$. Of particular interest is the relative strength of inter-dimer exchange, which determine the possible types of long-range magnetic ordering, and ultimately the nature of the ground state. In order to investigate this, we carried out DFT calculations on models with different combinations of magnetic interactions between Ru^{4+} ions. We begin by noting that intra-dimer exchange could be either AFM or FM. In simple cases, direct magnetic exchange depends on the $M-M$ distance: shorter distances favour AFM exchange while dimers with longer distances will relax to an FM state. Inter-dimer exchange could involve either: FM 180° and FM 90° exchange (FM); AFM 180° and FM 90° exchange (AFM); or AFM 90° exchange, which results in a frustrated AFM model (FAFM) regardless of the sign of the 180° exchange. This gives the 6 combinations of magnetic structure shown in Figure 6. Note that the frustrated inter-dimer (FAFM) cases are necessarily only approximations to frustration in a finite supercell.

Single-point energy (SPE) spin-polarised calculations to optimise the magnetic structures of these 6 models were carried out using a $2 \times 1 \times 1$ supercell of the experimentally determined unit cell at 1.5 K. The initial calculations used no Hubbard correction and a $2 \times 2 \times 2$ k-grid.

Results are shown in Table I. All AFM intra-dimer models were of lower energy than FM intra-dimer models, suggesting that AFM intra-dimer interactions are preferred. This is consistent with the experimental temperature dependence of magnetic susceptibility data above T^* [8].

Geometry optimisation (GO) calculations were then carried out to investigate whether the unit cell parameters change appreciably in the different magnetic models, and whether this affects their relative energies. These calculations used the same $2 \times 1 \times 1$ supercell, with no Hubbard correction and a $2 \times 2 \times 2$ k-grid. The results are included in Table I. Note that for the FAFM models, the approximate $2 \times 1 \times 1$ supercell allowed the frustration to be resolved by setting the spins on one "row" (along a) to zero. This created an artificial "stripe" superstructure; consequently, one should not directly compare the calculated energies of an FAFM inter-dimer model in which half the Ru atoms have spins to those of an FM or AFM

Intra/inter	F_{exp} (eV)	F_{opt} (eV)	$2a$ (Å)	b (Å)	c (Å)	β (°)	|Ru-Ru| (Å)	|Ru-O-Ru| (°)
Experimental			11.867	10.214	14.801	91.68	2.572	79.25
FM/FAFM	1.033	0.937	12.040	10.387	14.889	91.92	2.525	76.22
FM/FM	0.990	0.530	12.053	10.403	14.841	91.81	2.503	75.22
FM/AFM	0.896	0.466	12.055	10.409	14.840	91.79	2.505	76.92
AFM/FAFM	0.571	0.667	12.039	10.386	14.910	91.94	2.542	76.79
AFM/FM	0.116	0.089	12.051	10.398	14.885	91.86	2.532	76.28
AFM/AFM	0	0	12.052	10.398	14.880	91.88	2.534	76.75

TABLE I. Calculated energies (relative to the lowest energy state) of experimental and geometry optimised $2 \times 1 \times 1$ supercells with different combinations of signs of intra-dimer and inter-dimer interactions. F_{exp} refers to calculations using the experimentally determined unit cell; F_{opt} refers to the results of geometry optimisation calculations, the supercell parameter and key intradimer geometries for which are tabulated.

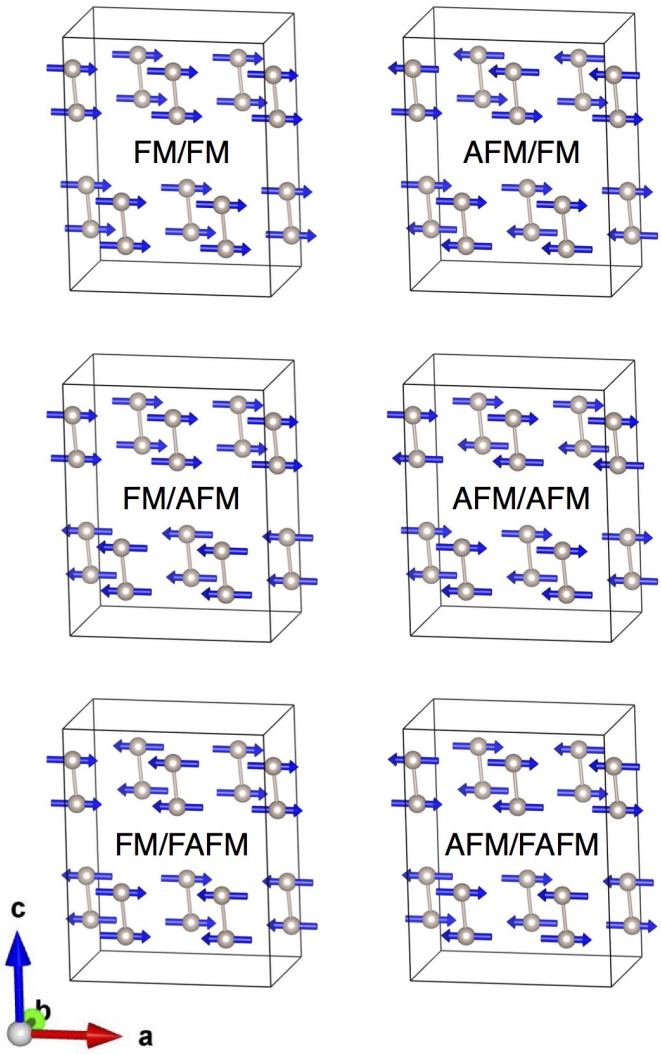

FIG. 6. Starting models for different magnetic configurations in a $2 \times 1 \times 1$ supercell of $Ba_3BiRu_2O_9$ used for DFT calculations. Only Ru sites are shown, with Ru-Ru intradimer bonds drawn.

inter-dimer model in which all Ru ions have spins. The range of relative energies for the optimised models was found to be smaller than for the unoptimised models, but the AFM/AFM model was the best behaved and lowest energy. The AFM/AFM model also yielded the largest Ru-Ru distances and Ru-O-Ru angles, closest to experimental values.

Based on these results, we used the $2 \times 1 \times 1$ supercell with experimental cell parameters to carry out systematic calculations on each of the models with net AFM interactions (noting that a fully FM model was clearly ruled out by magnetic property measurements [8]). These calculations were designed to obtain energies for the exchange constants J_0 (intra-dimer) and $J' = |2J_1 + 4J_2 + J_3 + J_4 + J_5|$ (inter-dimer), as shown in Figure 1(b). Two approaches were used. Firstly, the energies of the ordered cells were compared, noting that the $2\times1\times1$ supercell contains 8 dimers so that $E_{AFM/AFM} - E_{FM/AFM} = 8J_0$ and $E_{AFM/AFM} - E_{AFM/FM} = 16J'$. Secondly, two types of defects were introduced: flip one spin only ($D1 = J_0 + J'$); or flip both spins in a dimer ($D2 = 2J'$). These calculations were all performed for a range of values of the Hubbard U (using a fixed Hubbard $J = 1$) in order to investigate its influence on the relative energies. The defect approach yielded independent values for each of the three net AFM models, the mean of which is shown together with the results of the first approach in Figure 7. Negative values indicate AFM interactions. The two approaches show good agreement and the same behaviour as a function of $U - J$.

The results are shown in Fig. 7. Intra-dimer exchange J_0 is AFM for $U - J < 2.2$ and FM for $U - J > 2.2$. Inter-dimer exchange J' also crosses over from AFM to FM as $U - J$ increases, but at higher $U - J = 2.8$.

Finally, in order to test the possibility that the unusual apparent "4+" oxidation state of bismuth plays a direct role in the magnetic structure, we checked the final charge distribution in the s-shell on Bi, as a function of the magnetic ordering on the Ru sites. We found no evidence for any excess spin on "Bi^{4+}", suggesting that if it does exist, it is distributed across neighbouring O sites. We acknowledge, however, that there might be an effect due to the pseudo-potential used to model the semi-core (5d) states of Bi.

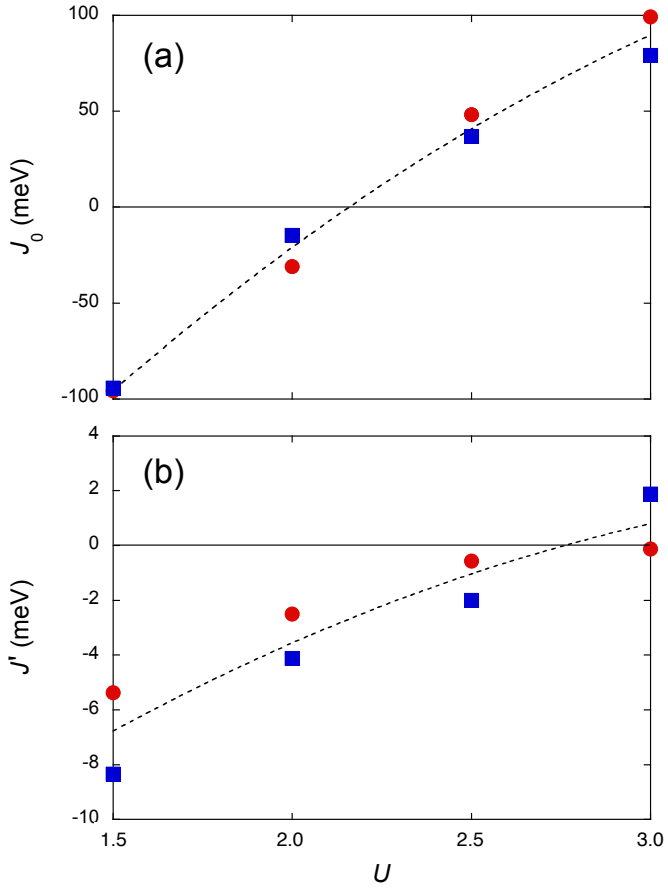

FIG. 7. (a) J_0 and (b) J' vs Hubbard ($U - J$) from DFT calculations. Red circles were determined by comparing the energies of different ordered cells; blue squares were determined by comparing defect energies; black dashed lines are 2nd-order polynomial fits.

D. X-ray Total Scattering Analysis

Our *ab initio* calculations described above point to a geometrically frustrated magnetic ground state and a lack of any change to the "Bi^{4+}" site (such as Bi^{3+}/Bi^{5+} charge disproportionation) below T^*. This is consistent with the absence of any change in space-group symmetry,[8] i.e., the absence of any type of long-range ordering associated with the transition. As a final check on the consistency of our experimental and computational results, we used x-ray total-scattering analysis to search for any evidence of short-range ordering.

Fig. 8 shows pair-distribution function (PDF) fits of the $C2/c$ structure of $Ba_3BiRu_2O_9$ to x-ray total-scattering data above (210 K) and below (130 K) $T^* = 176$ K. The fits are excellent in both cases, *i.e.*, there is no evidence for statistically significant local deviations from the long-range crystallographic average structure along the lines of the charge ordering observed in 6H-type $Ba_3NaRu_2O_9$.[30] This agrees with our diffraction results [8] which found no evidence for static disorder (changes in atomic displacement parameters) or strain (changes in peak widths) through T^*.

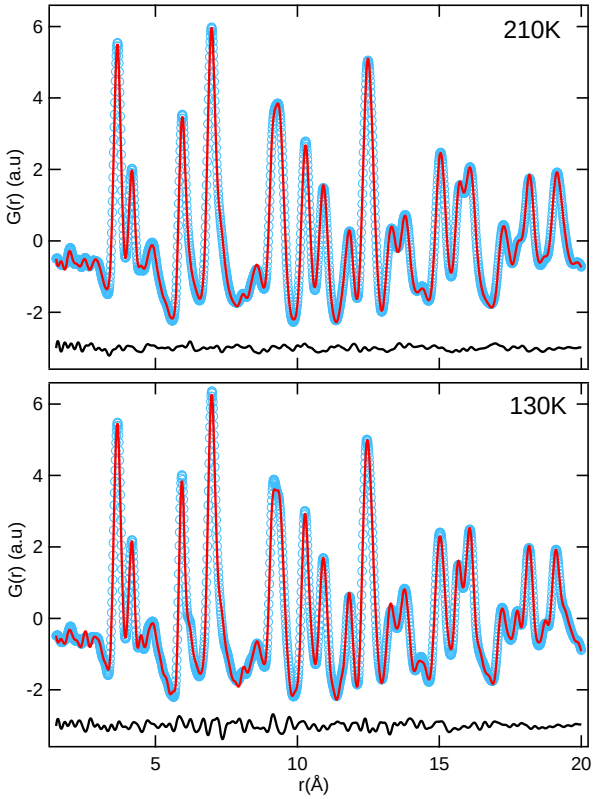

FIG. 8. PDF fits of the average $C2/c$ structure of $Ba_3BiRu_2O_9$ to SXRD data above (210 K) and below (130 K) $T^* = 176$ K.

Fig. 9 shows a contour map in the low r region that includes all the nearest-neighbor M-O bond lengths, which are indicated on the figure. There is no evidence for either Bi^{3+}/Bi^{5+} or Ru^{4+} charge disproportionation; and certainly no significant change in the nature of those ions above *vs.* below T^*. Hence we can rule out local charge ordering as the origin of the magnetostructural transition at T^*. The most obvious change at T^* concerns the Ba-O bonds, which cannot be directly involved in the magnetostructural transition, given that Ba^{2+} is not magnetic and that its oxidation state is unambiguous; the increased range of Ba-O bond lengths below T^* is consistent with the expanded unit cell and the high coordination number of Ba (see Fig. 1). There does, however, appear to be a slight broadening of the peaks corresponding to the Ru-Ru, Ru-O and Bi-O bonds below T^*. This is consistent with the onset of a frustrated AFM state that creates a range of local magnetostrictive environments.

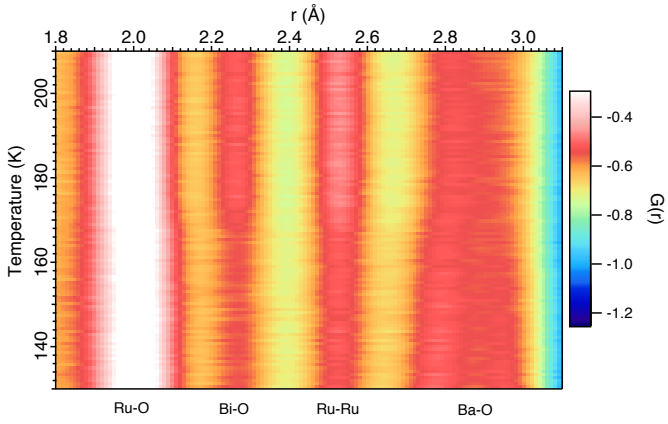

FIG. 9. Contour map of the radial distribution function of $Ba_3BiRu_2O_9$ at low r as a function of temperature, from SXRD data. Nearest-neighbor M-O bond lengths are labelled.

IV. DISCUSSION

From our previous analysis of temperature dependent magnetic susceptibility data for $Ba_3BiRu_2O_9$ [8], intradimer exchange is AFM above T^*. There was no evidence that this changes below T^*, and the presence of AFM dimers in the low-temperature regime is consistent with the observation by INS in this work of a spin-gap excitation. Associating the experimental value of this spin gap (36.03 ± 0.14 meV) with the singlet-triplet excitation ($\Delta E = J_0$) gives us $J_0 = -36$ meV. This allows us to identify the appropriate value of the Hubbard parameter in our *ab initio* calculations from Fig. 7(a) as $U - J = 1.9$, which in turn yields a calculated estimate of the inter-dimer exchange constant $J' = -4.2$ meV from Fig. 7(b).

At this point we must revisit the possibility, raised in Sections I and III.A, that the pairwise dimer interactions responsible for the spin gap excitation could be occurring between, rather than within, the structural Ru_2O_9 dimer units. In addition to the fact that the spin-gap model fits our INS data better for a short intra-dimer interaction, our calculations are inconsistent with the long inter-dimer scenario. This scenario would require the structural dimers to be FM, with a net spin moment; but the inter-dimer exchange constant J' is only positive for $U - J > 2.2$. Furthermore, the geometrically frustrated disposition of Ru_2O_9 dimers means that pairwise dimerization among them would result in local variations from the crystallographic average structure; something effectively ruled out by our total scattering analysis (Fig. 9). We are therefore satisfied that the spin-gap excitation is associated with intra-dimer exchange.

These combined experimental and computational results are consistent with the lack of observable long-range magnetic ordering at low temperatures, despite the strong intra-dimer AFM exchange $J_0 = -36$ meV being equivalent to $J_0/k_B = 420$ K. The temperature at which the magnetic susceptibility drops dramatically, $T^* = 176$ K, corresponds to the much weaker inter-dimer AFM exchange locking the relative spins of the dimers in place. However, even below this temperature, long-range magnetic ordering is prevented because AFM exchange in the $a-b$ plane results in geometric frustration on the almost perfectly triangular lattice of Ru_2O_9 dimers.

Having established the nature of the magnetic ground state of $Ba_3BiRu_2O_9$, and unequivocally linked the emergence of that ground state on cooling to the magnetostructural transition at $T^* = 176$ K (see the order parameter in Fig. 3(b)), we can consider the relationship between the structural and magnetic degrees of freedom in that transition. Experimentally, [8], we observe a $\sim 0.3\%$ c-axis expansion on cooling through T^*. From Table I, the frustrated AFM/FAFM model has the longest c axis of all the magnetic models for which GO calculations were performed. In particular, the c-axis is expanded by $\sim 0.2\%$ *vs.* the AFM/FM and AFM/AFM models, to which it should be compared given that our proposed scenario for the transition involves AFM intradimer interactions both above and below T^*. Our computational results are therefore consistent with prior crystallographic results. Our XANES data (Fig. 5) indicate increased localization of electron density in the t_{2g} orbitals of low-spin Ru^{4+} (d^4) ions below T^*, consistent with a reinforcement of the intra-dimer exchange below T^*, contributing to the magnetostructural effect.

V. CONCLUSION

Our computational results indicate that the magnetic properties of $Ba_3BiRu_2O_9$ are dominated by AFM intradimer exchange. This is consistent with our observation by magnetometry and inelastic neutron scattering (INS) experiments of a spin-gap excitation, which we can attribute to the transition from an $S_{dimer} = 0$ singlet ground state to an $S_{dimer} = 1$ triplet excited state. The measured value of 36.03 ± 0.14 meV corrects, but compares favourably to, the previous estimate based on bulk property measurements (19.0 ± 0.3 meV[8]). We also see spectroscopic evidence for a reinforcement of intra-dimer exchange below T^*, contributing to the spin-gap opening. These results unequivocally link the emergence of the gapped ground state to the magnetostructural transition on cooling below $T^* = 176$ K. However, we see no evidence for long-range magnetic ordering at low temperatures, reflecting the geometrically frustrated nature of the triangular Ru_2O_9 dimer lattice. Further work may seek to extend this analysis to $Ba_3BiIr_2O_9$, but this will be very challenging, because in the absence of experimental INS data (which appear to be unobtainable due to the neutron form factor of Ir) there is no obvious way of ensuring the validity of any calculations.

[1] M. Hase, I. Terasaki, and K. Uchinokura, Phys. Rev. Lett. **70**, 3651 (1993).

[2] G. M. Luke, Y. Fudamoto, K. M. Kojima, M. I. Larkin, J. Merrin, B. Nachumi, Y. J. Uemura, Y. Maeno, Z. Q. Mao, Y. Mori, H. Nakamura, and M. Sigrist, Nature (London) **394**, 558 (1998).

[3] P. Khalifah, K. D. Nelson, R. Jin, Z. Q. Mao, Y. Liu, Q. Huang, X. P. A. Gao, A. P. Ramirez, and R. J. Cava, Nature (London) **411**, 669 (2001).

[4] S. Lee, J.-G. Park, D. T. Adroja, D. Khomskii, S. Streltsov, K. A. McEwen, H. Sakai, K. Yoshimura, V. I. Anisimov, D. Mori, R. Kanno, and R. Ibberson, Nature Materials **5**, 471 (2006).

[5] C. D. Ling, B. J. Kennedy, Q. Zhou, J. R. Spencer, and M. Avdeev, J. Solid State Chem. **183**, 727 (2010).

[6] W. Miiller, M. Avdeev, Q. Zhou, B. J. Kennedy, N. Sharma, and C. D. Ling, J. Amer. Chem. Soc **134**, 29 (2012).

[7] J. Darriet, R. Bontchev, C. Dussarrat, F. Weill, and B. Darriet, Eur. J. Solid State Inorg. Chem. **30**, 287 (1993).

[8] W. Miiller, M. Avdeev, Q. Zhou, A. J. Studer, B. J. Kennedy, G. J. Kearley, and C. D. Ling, Phys. Rev. B **84**, 220406 (2011).

[9] Y. Doi and Y. Hinatsu, J. Phys.: Condens. Matter **16**, 2849 (2004).

[10] Y. Doi, M. Wakeshima, Y. Hinatsu, A. Tobo, K. Ohoyama, and Y. Yamaguchi, J. Mater. Chem. **11**, 3135 (2001).

[11] B. Schüpp-Niewa, L. Shlyk, Y. Prots, R. Niewa, and G. Krabbes, Z. Anorg. Allg. Chem. **632**, 572 (2006).

[12] D. E. Cox and A. W. Sleight, Solid State Commun. **19**, 969 (1976).

[13] G. Thornton and A. J. Jacobson, Acta Crystallogr., Sect. B: Struct. Sci. **34**, 351 (1978).

[14] A. Balzarotti, A. P. Menushenkov, N. Motta, and J. Purans, Solid State Commun. **49**, 887 (1984).

[15] C. Chaillout, P. Santoro, A. Remeika, A. S. Cooper, G. P. Espinosa, and M. Marezio, Solid State Commun. **65**, 1363 (1988).

[16] W. R. Flavell, M. Mian, A. J. Roberts, J. F. Howlett, M. M. Sarker, P. L. Wincott, R. L. Bilsborrow, and G. van Dorssen, J. Mater. Chem. **7**, 357 (1997).

[17] B. J. Kennedy, C. J. Howard, K. S. Knight, Z. Zhang, and Q. Zhou, Acta Crystallogr. Sect. A **62**, 537 (2006).

[18] G. Kresse and J. Furthmüller, Phys. Rev. B **54**, 11169 (1996).

[19] G. Kresse and D. Joubert, Phys. Rev. B **59**, 1758 (1999).

[20] T. E. Dann, S. C. Chung, L. J. Huang, J. M. Juang, C. I. Chen, and K. L. Tsang, J. Synchrotron Rad. **12**, 664 (1998).

[21] B. Ravel and M. Newville, J. Synchrotron Rad. **12**, 537 (2005).

[22] A. P. Hammersley, S. O. Svensson, M. Hanfland, A. N. Fitch, and D. Hausermann, High Pressure Research **14**, 235 (1996).

[23] P. Juhas, T. Davis, C. L. Farrow, and S. J. L. Bilinge, J. Appl. Cryst. **46**, 560 (2013).

[24] C. L. Farrow, P. Juhas, J. W. Liu, D. Bryndin, E. S. Božin, and J. C. R. Bloch, J. Phys.: Condens. Matter **19**, 335219 (2007).

[25] H. A.Furrer, Phys. Rev. Lett. **39**, 657 (1977).

[26] N. G. Parkinson, P. D. Hatton, J. A. K. Howard, C. Ritter, F. Z. Chien, and M.-K. Wu, J. Mater. Chem. **13**, 1468 (2003).

[27] Z. Hu, H. von Lips, M. S. Golden, J. Fink, G. Kaindl, F. M. F. De Groot, S. Ebbinghaus, and A. Reller, Phys. Rev. B. **61**, 5262 (2000).

[28] R. S. Liu, L. Y. Jang, H. H. Hung, and J. L. Tallon, Phys. Rev. B. **63**, 212507 (2001).

[29] P. E. Blanchard, Z. Huang, B. J. Kennedy, S. Liu, W. Miiller, E. Reynolds, Q. Zhou, M. Avdeev, Z. Zhang, J. B. Aitken, B. C. Cowie, L.-Y. Jang, T. T. Tan, S. Li, and C. D. Ling, Inorg. Chem **53**, 952 (2014).

[30] S. A. J. Kimber, M. S. Senn, S. Fratini, H. Wu, A. H. Hill, P. Manuel, J. P. Attfield, D. N. Argyriou, and P. F. Henry, Phys. Rev. Lett. **108**, 217205 (2012).